

## Cirrus cloud optical, microphysical, and radiative properties observed during the CRYSTAL-FACE experiment: A lidar-radar retrieval system

C. Mitrescu,<sup>1</sup> J. M. Haynes,<sup>2</sup> G. L. Stephens,<sup>2</sup> S. D. Miller,<sup>1</sup> G. M. Heymsfield,<sup>3</sup> and M. J. McGill<sup>3</sup>

Received 15 November 2004; revised 3 February 2005; accepted 23 February 2005; published 13 May 2005.

[1] A method of retrieving cloud microphysical properties using combined observations from both cloud radar and lidar is introduced. The description of the lidar-radar model accounts for nonspherical effects of the ice crystals, with a treatment for multiple scattering and Mie effects. This retrieval makes use of an improvement to the traditional optimal estimation retrieval method, whereby a series of corrections are applied to the state vector during the search for an iterative solution. This allows faster convergence to a solution and is less processor intensive. The retrieval method is applied to radar and lidar observations from the CRYSTAL-FACE experiment, and vertical profiles of ice crystal characteristic diameter, number concentration, and ice water content are retrieved for a cirrus cloud layer observed 1 day of that experiment. Empirical relationships between ice water content and radar reflectivity as well as between particle number concentrations and characteristic diameter are also examined. The results indicate that a distinct and robust relationship exists between the latter two parameters, offering insight into the nature of cirrus microphysical processes.

**Citation:** Mitrescu, C., J. M. Haynes, G. L. Stephens, S. D. Miller, G. M. Heymsfield, and M. J. McGill (2005), Cirrus cloud optical, microphysical, and radiative properties observed during the CRYSTAL-FACE experiment: A lidar-radar retrieval system, *J. Geophys. Res.*, 110, D09208, doi:10.1029/2004JD005605.

### 1. Introduction

[2] Processes relating to the atmospheric branch of the hydrological cycle play an especially critical role in climate change especially through cloud and water vapor feedbacks [Stephens, 2005; Held and Soden, 2000]. Understanding and ultimately quantifying these cloud feedbacks remains a significant obstacle in climate research. Furthermore, the role of cirrus clouds in such feedbacks have been specifically called out in a number of studies [e.g., Ramanathan and Collins, 1991; Lindzen et al., 2001; Hartmann and Larson, 2002, and references therein]. The issues underpinning cloud feedback generally can be cast in the form of the following questions [e.g., Stephens, 2002]: (1) Given a fixed distribution of clouds and relevant properties, what are the effects on radiative heating? (2) Given a fixed distribution of heating, what then is the influence on clouds? While our understanding of the radiative transfer processes are sufficiently advanced, our inability to specify the relevant properties of cirrus clouds precludes straightforward answers to the first question. Specifying

the cloud properties is also a necessary step for addressing the second more difficult question that requires a clearer understanding of how the heating and moistening effects of clouds in turn feed back to influence the dynamical and thermodynamical properties of the atmosphere, and subsequently the large-scale motions of air driving the formation and evolution of cirrus clouds themselves. Given these outstanding problems, prediction of the formation and evolution of clouds is poorly handled in models and our ability to test these predictions with global cloud observations is also limited.

[3] Since cirrus clouds are ubiquitous [Liou, 1986] and their bulk microphysical properties highly variable [e.g., Heymsfield, 1972], satellite remote sensing methods are important for studying the influence of cirrus on the global climate system. The verification of these methods is also of critical importance. Unfortunately, such verification suffers from a relative dearth of in situ ice cloud measurements and limited campaigns to collect such data matched to the observations.

[4] This paper presents a remote sensing procedure defining the properties of cirrus clouds that potentially could be used to address the first broad question posed above. The procedure combines lidar and radar measurements to estimate vertical profiles of cirrus cloud microphysical properties that are required to define the effects of these clouds on the radiation budget. The specific properties of interest are the intensive properties of size distribution, concentration, and geometry of ice or water droplets within the clouds, and

<sup>1</sup>Marine Meteorology Division, Satellite Meteorological Application Section, Naval Research Laboratory, Monterey, California, USA.

<sup>2</sup>Department of Atmospheric Science, Colorado State University, Fort Collins, Colorado, USA.

<sup>3</sup>NASA Goddard Space Flight Center, Greenbelt, Maryland, USA.

the extensive properties of cloud geometric shape and thickness. The physical basis for such an approach was first explored by *Intrieri et al.* [1993] and has more recently been pursued in the work of *Donovan and van Lammeren* [2001] among others. Here we formulate the retrieval problem in terms of an optimal estimation framework [Jazwinsky, 1970; Rodgers, 2000] as introduced by *Stephens et al.* [2001] and followed by a series of similar papers [e.g., *Heidinger and Stephens*, 2000; *Austin and Stephens*, 2001; *Miller et al.*, 2001; *Cooper et al.*, 2003]. The present work modifies the traditional optimal estimation technique to increase computational efficiency for systems represented by large retrieval vectors and hastens convergence to a solution. The lidar-radar retrieval algorithm is described in section 3. The method is then applied to data collected during the CRYSTAL-FACE campaign that occurred in south Florida during July 2002. Retrieved optical and microphysical parameters are validated against in situ measurements.

## 2. A New Implementation of the Optimal Estimation Problem

[5] The general problem of determining the state of a system from noisy measurements is called estimation, or filtering. A key component of the estimation problem is the specification of a physical model that relates the measurements to the state variables, referred to as the forward model or the mapping operator. The most probable system state described by such a model is the one that minimizes the cost function. Under the assumption of Gaussian statistics [Jazwinsky, 1970], and by ignoring the a priori term (a reasonable assumption for the present application), we can write this cost function as

$$J(\mathbf{x}) = \frac{1}{2} [\mathbf{y} - \mathbf{H}(\mathbf{x}, \mathbf{b})]^T \mathbf{R}^{-1} [\mathbf{y} - \mathbf{H}(\mathbf{x}, \mathbf{b})], \quad (1)$$

where  $\mathbf{x}$  represents the state vector of the system,  $\mathbf{y}$  expresses the measurement or constraint vector,  $\mathbf{H}$  is the (nonlinear) forward model,  $\mathbf{R}$  is the observation covariance matrix, and  $\mathbf{b}$  is the forward model vector of parameters. Here, a constraint is referred to as an integrated property of the system, such as the optical depth, ice water path, mean temperature, etc. The forward model vector of parameters is a list of unretrieved physical variables needed in the description of the forward model. They are being held constant, although some of them may display some variability/uncertainty within the measurements. We define one component of the state vector by  $x_m$ , where  $m$  identifies the physical variable. As discussed later, this can be either particle number concentration, particle size, or lidar ratio at a specific location within the cloud. The dimension of the state vector is the sum of all its variables (chose here to match the numbers of measurements/constraints  $L$ ). The solution to our current problem is given by

$$A_{mk} \delta x_k = G_m \quad m, k = 1, \dots, M, \quad (2)$$

with

$$A_{mk} = \sum_{sq} \frac{\partial H_s}{\partial x_m} R_{s,q}^{-1} \frac{\partial H_q}{\partial x_k} \quad (3)$$

and

$$G_m = \sum_{sq} \frac{\partial H_s}{\partial x_m} R_{s,q}^{-1} [y_s - H_s(\mathbf{x}_0)], \quad (4)$$

where  $M$  is the dimension of a subset of components of the state vector, and  $\mathbf{x}_0$  is the state vector determined at a previous iteration step. In order to complete the minimization process, the above procedure must be applied to the next subset of components of the state vector until all components of the state vector are adjusted. The advantage of the present formulation over the more common approach (that sets  $M = L$  and all state vector components are varied simultaneously) lies in its reduced dimension. Such a reduction is crucial for data assimilation problems, where dimensions of the order of  $10^7$  are typical. It is also helpful for highly nonlinear problems, when  $\mathbf{A}$  and  $\mathbf{G}$  matrices must be evaluated at each iteration step. Finally, the choice for the number of elements  $M$  depends strongly on the forward model  $\mathbf{H}$  and dimension  $L$ . A qualitative discussion regarding these issues is given at the end of the next section.

[6] An important aspect of the optimal estimation method resides in the computation of error covariance matrix of the state vector. Our basic assumption is that of Gaussian error statistics. When these errors are small, this is a valid assumption and a tangent linear model can be applied to solve the system. When dealing with nonlinear forward models with potentially large measurement and/or model parameter errors, however, the state vector errors are no longer symmetric with respect to the mean. Thus the error statistics should only be seen as an estimate. Without entering details [see *Austin and Stephens*, 2001], the errors of our retrieved state vector can be evaluated using the error covariance matrix  $\mathbf{S}$ , written as

$$\mathbf{S}^{-1} = \left( \frac{\partial \mathbf{H}}{\partial \mathbf{x}} \right)^T \mathbf{R}^{-1} \left( \frac{\partial \mathbf{H}}{\partial \mathbf{x}} \right), \quad (5)$$

which is just the  $\mathbf{A}$  matrix at full dimension, since we neglected the a priori error covariance matrix from our cost function definition. The diagonal elements of  $\mathbf{S}$  are variances of the state vector and thus give a measure of the uncertainty in the retrieval; off-diagonal elements are cross-correlation errors between components. For the purpose of estimating the above errors, the observation error covariance matrix  $\mathbf{R}$  contains both measurement errors as well as errors due to uncertainty in forward model parameters  $\mathbf{b}$ . All these errors are assumed to be uncorrelated. More details about the evaluation of errors in the retrieval are given below.

## 3. Formulating the Lidar-Radar Retrieval Problem

[7] This section describes how the general retrieval method presented above is applied to lidar and radar measurements to infer cloud optical and microphysical parameters. The first stage in the application is to define the forward model through analytical expressions relating the state vector (i.e., physical variables) to the measured vector (i.e., measured quantities). Since the measurements pertain to a cloud composed of complex particles, we

begin by defining a characteristic function describing the cloud microphysical properties. Then, using specific principles of radiative transfer theory, we define a relationship between the state vector and each of the measured fields. The ensemble of all these equations, valid within some specific range of state vector space, comprise our forward model. This section begins with an introduction of our microphysical approximations, then defines the lidar and radar model, and closes with a discussion of sensitivity and limitations.

### 3.1. Microphysical Model

[8] In situ microphysical observations of cirrus clouds reveal that ice particles display a wide variety of complex shapes and dimensions with a strong dependence on dynamical and thermodynamical factors [Heymsfield *et al.*, 2002a]. However, despite this increased complexity, for radiative purposes we can rely on averaged particle properties which were shown to be more suitable for an analytical description. Following examples set by previous studies [Verlinde *et al.*, 1990; Matrosov *et al.*, 2003] we assume a fixed form of the size distribution, described by a number of parameters characterizing its shape. In this case we assume a Gamma size distribution for the cloud particles with diameter  $D$ :

$$n(D) = N_0 \frac{1}{\Gamma(\nu)} \left(\frac{D}{D_0}\right)^{\nu-1} \frac{1}{D_0} \exp\left(-\frac{D}{D_0}\right). \quad (6)$$

Both the characteristic diameter  $D_0$  (mm) and particle concentration  $N_0$  (number per liter) are functions of position in the cloud. Given the characteristics of our observing system, we assume that the width parameter  $\nu$  is a constant throughout the cloud (i.e., a forward model parameter). In the above representation, diameter  $D$  represents the maximum dimension of a particle as measured by an imaging probe. This defines what is referred to as an equivalent sphere. Of relevance to remote sensing observing systems, are the means of projected area, volume and mass of ice cloud particles. Since these quantities must be derived from the above form of distribution, in the case of nonspherical particles, we must also define some area-, volume-, and mass-diameter relationships. Empirical fits to measured data, exemplified throughout the literature [e.g., Brown and Francis, 1995; Francis *et al.*, 1998; Mitchell *et al.*, 1996], approximate these relationships as power laws of the form

$$X(D) = g_X D^{f_X}, \quad (7)$$

where  $X$  is the variable of interest (area, volume, mass, density, etc.) and  $g_X$  and  $f_X$  are cloud-averaged fit coefficients. The mean values of  $X$  can then be expressed as

$$\langle X \rangle = \int_0^\infty X(D) n(D) dD = \frac{\Gamma(\nu + f_X)}{\Gamma(\nu)} N_0 X(D_0). \quad (8)$$

Heymsfield *et al.* [2002b] demonstrate an application of such averaged properties. Their fit coefficients show a large range of variation over the multitude of observed cirrus clouds. In order to correctly estimate any of the above mean values, parameters  $\nu$ ,  $f_X$ , and  $g_X$  must be known. These coefficients are usually habit- and temperature-dependent, but for the purpose of this study they are considered fixed; their mean

values are adapted from the work of Heymsfield *et al.* [2004a, 2004b]. An important simplification to the above formulation arises when we considered all ice particles of a particular given shape, in which case the fit coefficients  $g_X$  and  $f_X$  become universal. For spheres, the cross sectional area is given by  $g_A = \pi/4$  and  $f_A = 2$ , and volume is given by  $g_V = \pi/6$  and  $f_V = 3$ . The introduction of a spherical shape assumption is not arbitrary. Most of the radiative transfer (RT) calculations are made under this simplified assumption since we can always consider an “equivalent” medium with such properties. Ice crystal mass can be treated in a similar way, leading to the concept of ice crystal effective density [e.g., Heymsfield *et al.*, 2004a]. Thus the diameter  $D^{(s)}$  of an “equivalent solid sphere,” with fixed density  $\rho_i = 918 \text{ kg m}^{-3}$ , having the same mass or ice water content (IWC) as a complex geometry ice crystal with maximum dimension  $D$ , is defined as

$$D^{(s)} = \left(\frac{\bar{\rho}}{\rho_i}\right)^{1/3} D, \quad (9)$$

where  $\bar{\rho}$  is the ice particle effective density. We note that the ratio between the effective and solid ice densities defines the ice fraction. Following the arguments presented above, we construct our forward models based on the assumption of equivalent spheres of maximum diameter, while the nonspherical effects are expressed by values of coefficients  $g_X$  and  $f_X$ .

[9] In the following subsections we introduce our forward models and define the state and measurement vectors. Whenever necessary, information regarding the above microphysical description is applied.

### 3.2. Lidar Model

[10] For the lidar system, the attenuated backscatter at some level  $z$  can be expressed as [Weitkamp, 1999; Mitrescu, 2005]

$$\beta'(z) = S^{-1} C \beta_{\text{ext}}(z) \exp\left[-2 \int_0^z \beta_{\text{ext}}(z') dz'\right], \quad (10)$$

where  $S$  is the lidar extinction-to-backscatter ratio (in sr),  $C$  is a factor describing the multiple scattering (MS) contribution, and  $\beta_{\text{ext}}$  is the extinction coefficient. The integral term describes the two-way attenuation of the lidar beam due to extinction processes. We note that molecular backscatter/attenuation is also taken into account, but for clarity this term is omitted from the lidar equation. Since the measured attenuated backscatter signal is originating from a finite conical atmospheric volume defined by the lidar field of view (FOV) and vertical resolution  $\delta z$  (in km), we integrate the above equation within  $z \pm \delta z/2$  finite layer limits to obtain

$$\beta'(i) [\text{km}^{-1} \text{sr}^{-1}] = \frac{C(i)}{2 S \delta z} \left[1 - e^{-2 \beta_{\text{ext}}(i) \delta z}\right] \cdot e^{-2\tau(i)}, \quad (11)$$

with

$$\tau(i) = \left[ \sum_{k=1}^{i-1} \beta_{\text{ext}}(k) \right] \cdot \delta z. \quad (12)$$

Here  $\tau(i)$  is the cloud optical depth to level  $i$ , which increases with lidar penetration depth; therefore the above definition is valid for both upward and downward looking lidars.  $S$ ,  $C$ , and  $\beta_{\text{ext}}$  are finite layer mean values, while neglecting absorption processes; this is a valid assumption at lidar wavelengths. For our lidar model description, the lidar ratio  $S$  (in sr), considered constant throughout the vertical cloud profile, is determined according to the technique described by *McGill et al.* [2003].

[11] As introduced above, given the divergence of the lidar's FOV and the distance between lidar and target, we must account for MS effects. However, for lidar FOV's sufficiently smaller than the angular width of the forward scatter peaks of the probed scatterers and close ranges values, the MS effects can be neglected [*Eloranta*, 1998]. Although there are many MS models to chose from [e.g., *Eloranta*, 1998; *Bissonnette*, 1988], all of them require a priori knowledge about cloud vertical structure, some of which cannot be retrieved within the present formulation. We refer here to the ice particles' scattering phase function. The lidar ratio  $S$ , a model parameter here, only gives information about the value of the phase function at backward scattering angles and not near forward angles as required by the MS models. One approach to solving this problem is to approximate the phase function at forward angles with that of a Gaussian function whose parameters are determined from the knowledge of particle effective diameter [*Eloranta*, 1998]. However, as shown later, this parameter cannot be retrieved without the addition of the radar system. Thus when lidar is to be used alone, assumptions about this model parameter must be made. For our purposes, we consider that the effective radius is fixed to 20  $\mu\text{m}$ , a value that is typical for radiative calculations of thin cirrus clouds. Thus MS effects are estimated as follows:

$$C(i) = \sum_{m=1} P_m(i) / P_1(i). \quad (13)$$

Here  $P_m$  represents the contribution to the backscatter signal from the  $m$ th order of scatter [*Eloranta*, 1998], which is a function of the cloud optical and microphysical properties, lidar FOV, and distance to target. The summation should be performed over as many scatter orders as needed for convergence. However, given the increased computational burden required by higher orders of scattering, most of the models stop at third-order scatter, which is a good approximation at low cloud optical depths. In order to avoid such a computational burden for our application, when iteratively converging toward a solution we initially estimate  $C$  by using a simple parameterization as proposed by *Mitreanu* [2005]. It is only at the last two iteration steps (i.e., when close to solution), that MS effects are evaluated using (13). At this point, MS contribution is evaluated up to fourth order of scatter. This approach clearly speeds up the convergence process, without losing accuracy when evaluating MS effects.

[12] When only lidar attenuated backscatter and information about the lidar ratio are available, as expressed by (11)–(13), the state vector is reduced in both dimension and information content. However, key cloud optical properties, such as the profile of the extinction coefficient, can still be inferred from such measurements. We can thus define the

measurement vector and the state vector associated with what we term a “ $\beta$  model” (that only uses information from the lidar system) in the form

$$\mathbf{y} = [\ln \beta'(1), \ln \beta'(2), \dots, \ln \beta'(n)] \quad (14)$$

$$\mathbf{x} = [\beta_{\text{ext}}(1), \beta_{\text{ext}}(2), \dots, \beta_{\text{ext}}(n)]. \quad (15)$$

We point out that the form of the  $\beta$  model requires no specification of the particle size distribution (with the exception of MS effects).

[13] In order to complete our lidar model, we note that at the nonabsorbing lidar wavelengths, the extinction efficiency, which equals the scattering efficiency, approaches the value of two [*Stephens*, 1994]. Use of the general expression (8) for defining the cross sectional area yields

$$\beta_{\text{sca,ext}}(i) [\text{km}^{-1}] = 2g_A \frac{\Gamma(\nu + f_A)}{\Gamma(\nu)} N_0(i) D_0^{f_A}(i), \quad (16)$$

where  $g_A$  and  $f_A$  are fitting coefficients describing cross sectional area as a function of diameter for our nonspherical ice particles. As mentioned above, while smaller ice particles can be considered spheres, larger ice particles display a highly irregular shape; we thus expect  $g_A$  to be less than  $\pi/4$ , while  $f_A$  is less than two. In anticipation of our case study, where small ice crystals were dominant, we choose the following values:  $g_A = 0.55$  and  $f_A = 1.9$  [*Heymsfield et al.*, 2004a, 2004b]. We note that it is at this point that nonspherical effects are revealed, underlying the idea that these effects are defined and characterized at the microphysical level. Cloud optical properties (extinction coefficient, optical depth, lidar ratio), as determined by the lidar system alone, although influenced by nonsphericity, cannot reveal such a structure in the absence of an explicit formulation. This is clearly explained by the above form of the state vector (15).

### 3.3. Radar Model

[14] For Rayleigh scattering, the backscatter cross section is proportional to the square of the product between the scalar average volume polarizability and the volume (excluding hollow regions) of the scatterer [*Donovan and van Lammeren*, 2001; *Heymsfield et al.*, 2002a]. Thus the radar reflectivity can be expressed as

$$\mathcal{Z}_R(i) [\text{mm}^6 \text{m}^{-3}] = g_Z \frac{\Gamma(\nu + f_Z)}{\Gamma(\nu)} N_0(i) D_0^{f_Z}(i), \quad (17)$$

where  $g_Z$  and  $f_Z$  are fit coefficients describing ice crystal nonspherical effects, and subscript  $R$  indicates Rayleigh approximation. Similar to our discussion of the extinction coefficient,  $g_Z$  is less than 1000, while  $f_Z$  is less than six. As mentioned above, in anticipation of a collection of ice crystals dominated by relatively small ice crystals, we choose  $g_Z = 350$  and  $f_Z = 5.2$  [*Heymsfield et al.*, 2004a, 2004b]. The values for these coefficients are due to values of fit coefficients of both cross sectional area and effective density, describing ice crystal nonspherical effects.

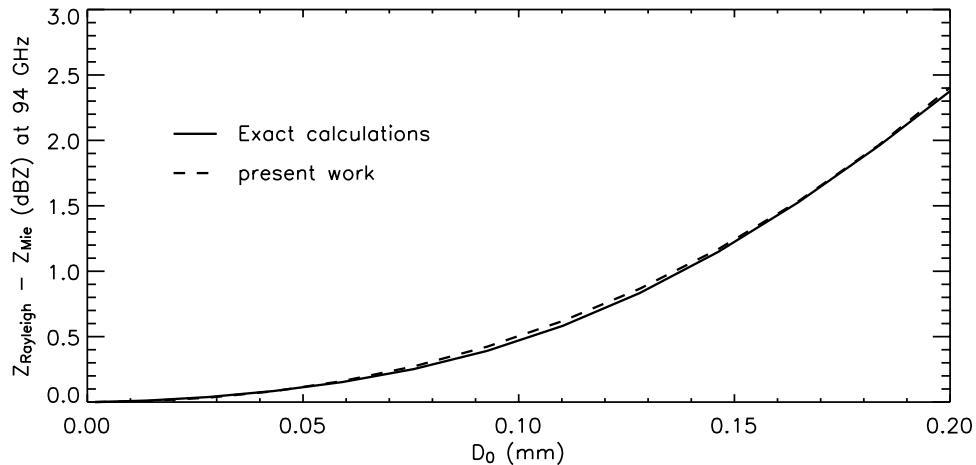


**Figure 1.** Differences between Rayleigh and Mie regimes for a 94 GHz radar plotted as a function of characteristic diameter  $D_0$ : exact calculations (solid line) and empirical fit (dashed line).

[15] Seeking a formulation equivalent to that of *Donovan and van Lammeren* [2001], we rewrite (17) in terms of (16) to yield (in dBZ units)

$$Z_R(i)[dBZ] = 10 \cdot \log_{10} \left[ \frac{g_Z}{2 g_A} \frac{\Gamma(\nu + f_Z)}{\Gamma(\nu + f_A)} \beta_{\text{ext}}(i) D_0^{f_Z - f_A}(i) \right]. \quad (18)$$

[16] However, in order to accurately compute radar reflectivities for larger ice crystals, state-of-the-art models should be used. Using Discrete-Dipole Approximation (DDA) calculations on various ice crystal shapes, *Donovan et al.* [2005] showed that for randomly oriented small ice crystals, the differences between Mie and DDA calculations are negligible and do not depend on the choice of the ice crystal equivalent size representation. Since DDA estimations are beyond the scope of the present paper, based on the above findings, we evaluate our corrections using Mie theory [*Bohren and Huffman*, 1983]. These calculations are specifically designed for collections of Gamma distributed ice crystals with characteristic maximum diameters less than 200  $\mu\text{m}$ . We estimate the expected differences between Rayleigh and Mie radar reflectivities by assuming a similar Gamma distribution of equivalent solid ice spheres at  $-20^\circ\text{C}$ , with  $\nu = 2$  [*Dowling and Radke*, 1990], thus conserving individual ice crystal mass. Then, using the expression for mass of the form (7), valid for our crystal size ranges, we simply express this correction in terms of  $D_0$ . From Figure 1 we notice that these differences become more accentuated for larger particles, with corrections larger than 2 dBZ when characteristic diameter  $D_0$  approaches 0.2 mm (solid line). Thus in order to account for Mie effects in our calculations, Rayleigh reflectivities (18) must be adjusted by the following term (in dBZ):

$$M = 100 \cdot D_0^2 \cdot (0.4 + D_0), \quad (19)$$

where  $D_0$  is expressed in mm (dash line in the figure). In conclusion, the formulation of our radar model describing ice particles can be expressed as [*Heymsfield et al.*, 2002a]

$$Z_M(i) = Z_R(i) - 7.2 - M(i), \quad (20)$$

where index  $M$  indicates that Mie effects are accounted for, factor 7.2 is due to differences between ice and water dielectric constants, and it is assumed that attenuation due to water vapor is negligible. We acknowledge that the final estimate of the radar reflectivity is not entirely accurate since the fit coefficients  $g_Z$  and  $f_Z$  used are in fact temperature-, size-, and habit-dependent. Since such an explicit dependence is beyond the scope of this work, we consider all fit coefficients as stated and account for their uncertainty in the observation error covariance matrix.

[17] From (17)–(20), we note that contrary to the lidar model, the formulation of the radar model requires knowledge about the microphysical structure. Therefore this structure (namely  $N_0$  and  $D_0$ ) cannot be retrieved at each level using this formulation. However, by adding information from the lidar system, such a task is possible.

### 3.4. Forward Model: $Z - \beta$ Algorithm

[18] The lidar and radar backscatter ice particles properties expressed by (11)–(13), (16), and (18)–(20), constitute what we call the “ $Z - \beta$  model” as the forward model of the lidar-radar observing system. In order to profile cloud microphysical parameters, lidar and radar measurements are required at each cloud level. However, in the case of real measurements, such a perfect overlap is rarely achieved. For a down-looking observing system, we expect lidar to measure the top thin cloud layers that are missed by radar. As we will see later, this is often the case with thin cirrus that go undetected by the radar system but are observed by the lidar system. For lower, denser cloud layers, the lidar is attenuated, while radar signal gains in strength. As mentioned above, lidar system alone can provide information about cloud optical properties. The addition of radar observation enables the determination of the microphysical structure in terms of  $N_0$  and  $D_0$  in regions of lidar/radar overlap. Thus the measured and state vector can be defined as follows:

$$\mathbf{y} = [\ln \beta'(1), \ln \beta'(2), \dots, \ln \beta'(n), Z(1), Z(2), \dots, Z(n)] \quad (21)$$

$$\mathbf{x}(\nu) = [\beta_{\text{ext}}(1), \beta_{\text{ext}}(2), \dots, \beta_{\text{ext}}(n), D_0(1), D_0(2), \dots, D_0(n)], \quad (22)$$

where lidar and radar layers are identified by their indexes. Here we consider all  $n$  lidar layers, some of which are overlapped by radar. Therefore when radar signal is below the minimum detectable level, we default to the  $\beta$  model and set the characteristic diameter to a prespecified value (i.e.,  $D_0 = 10 \mu\text{m}$ ).

[19] Solving for the above form of the state vector follows the steps described in previous section. For the overlap region, once profiles of  $N_0$  and  $D_0$  are retrieved, profiles of ice water content (IWC) are obtained by simply integrating the individual mass particle over the particle size distribution. Using the mass-diameter relationship in the form (7), for the particle size distribution considered here, we can estimate the IWC as

$$\text{IWC}(i) [\text{mg m}^{-3}] = g_m \frac{\Gamma(\nu + f_m)}{\Gamma(\nu)} N_0(i) D_0^{f_m}(i). \quad (23)$$

As before, this expression accounts for nonspherical effects. Here, we set the values of the coefficients to  $g_m = 55$  and  $f_m = 2.6$ , which is valid for ice crystals with diameter less than  $200 \mu\text{m}$  [Heymsfield *et al.*, 2004b]. From the above equation, we can also estimate the ice water path (IWP) for the overlap region, as

$$\text{IWP} [\text{g m}^{-2}] = \sum_{i=1}^n \text{IWC}(i) \delta z. \quad (24)$$

[20] We thus conclude our lidar-radar forward model formulation and the definition of derived quantities that characterize both optical and microphysical properties of ice cirrus cloud, with a full description of ice particle nonspherical effects.

### 3.5. Initial Guess

[21] The approach described in section 2 can be used as a general method for solving systems of nonlinear equations when solutions for such systems exist. However, the number of iterations required for convergence to the solution depends on the initial guess of the state vector. In order to speed up the iterative process, the initial guess must be as close to the solution as possible. For this we can employ various techniques. A common procedure is to simplify the system of equations to a level that permits analytic solutions, later used as the initial guess  $\mathbf{x}_0$ .

[22] For the lidar model, when  $C$  is known, an analytical solution for the extinction coefficient is possible. From (11) we deduce

$$\beta_{\text{ext}}^*(i) = -\frac{1}{2 \delta z} \cdot \ln \left[ 1 - \frac{2 S \delta z \beta'(i) e^{2 \tau(i)}}{C(i)} \right]. \quad (25)$$

Although in an analytical form, the above equation is subject to the a priori knowledge of MS effects. A two step procedure is useful: first, we evaluate (25) by setting  $C = 1$ . Then, using the aforementioned parameterization, we evaluate the  $C$  term; further use of (25) yields an estimate of the extinction coefficient and an update of the optical depth is possible. It is clear that this procedure cannot yield the true solution; we expect a biased estimation at deeper cloud levels, where MS effects become important.

[23] When adding radar information to the lidar system, an analytical solution is again possible. From (16), (18), and (25) we can estimate characteristic diameter,

$$D_0^*(i) = \left\{ \frac{2 g_A}{g_Z} \frac{\Gamma(\nu + f_A)}{\Gamma(\nu + f_Z)} \frac{10^{[Z_M(i)]/10}}{\beta_{\text{ext}}^*(i)} \right\}^{1/(f_Z - f_A)}, \quad (26)$$

and particle number concentration,

$$N_0^*(i) = \frac{1}{2 g_A} \frac{\Gamma(\nu)}{\Gamma(\nu + f_A)} \beta_{\text{ext}}^*(i) [D_0^*(i)]^{-f_A}. \quad (27)$$

From the above set of equations (26) and (27), we note the nonlinear dependence on the value of the width parameter  $\nu$  and fit coefficients  $f_{A,Z}$ . This nonlinearity may be responsible for higher errors of our retrieved variables, since errors computed by the optimal estimation method (5) assume that an approximation of a tangent linear model is valid throughout the range of variability of a given variable or parameter. Therefore we can only have an estimate of the errors and not their exact values. Moreover, uncertainty of model parameters can also lead to biased results. It is thus desirable that their values be as accurate as possible.

[24] We note that the above expressions (25)–(27), although not the exact solutions to our observing system (hence the asterisk superscript), are useful when dealing with possible multiple solutions, since we can choose the most appropriate solution. It also eliminates the need for an a priori estimate and all the complicated algebra that follows. Also clear from the above approximation is that the analytical solution is obtained iteratively: we first determine  $\beta_{\text{ext}}$ , which requires additional iterative calculations involving cloud optical depth, then  $D_0$  and  $N_0$ . This supports our proposed algorithm where we iterate toward solution only for some of the state vector components at a time. We thus gain speed and accuracy without losing the generality offered by the optimal estimation formulation. Regarding our discussion in the previous section, given the form of the forward model (lidar system in particular) and the dimensions of the matrices involved in calculations of deep cloud profiles (with more than 100 vertical points possible), we choose sets of  $M = 10$  components of the state vector when employing the optimal estimation method. Other sets were tested, but for this particular problem, convergence was always obtained, which is a desirable way of improving the optimal estimation method when applied to lidar data [Stephens *et al.*, 2001].

[25] A schematic of the algorithm implementation using lidar and radar data is presented in Figure 2. Here we make use of our forward models, by properly identifying state and measurement vectors at each step. Various other measurements can be added to this schematic, provided that their formulations further detail the physical structure of the state vector. When such detail is achieved, some model parameters can be evaluated. Such is the case with the lidar system where MS effects are properly evaluated only after the addition of radar data, when information about the dimensions of the scattering particles becomes available. At the end of the cycle, the cost function is evaluated and tested against a prespecified threshold  $\epsilon$  and a decision is made. In our case,  $\epsilon$  is just the value of the cost function evaluated at

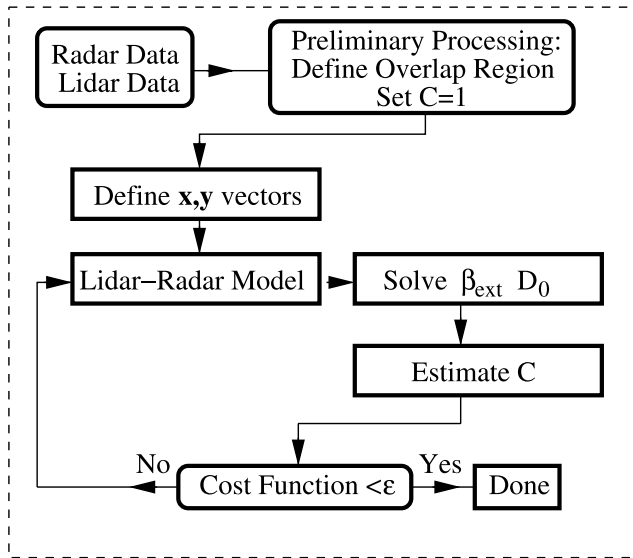


**Figure 2.** Schematic of the proposed algorithm. See text for details.

a previous iteration. We thus ensure that the solution is that which minimizes the proposed form of the cost function.

### 3.6. Width Parameter Dependencies

[26] In this subsection we offer an analysis of the dependence of our state vector components on the width parameter  $\nu$ . This is an important parameter describing the particle size distribution and is responsible for the nonlinear response for our lidar-radar model. In order to keep our analysis as simple as possible, we neglect both Mie and MS effects in our discussion. Then, from (23), (26), and (27) we can infer the dependence of the retrieved parameters with respect to  $\nu$ . Figure 3 shows the relative variation of the above variables with respect to  $\nu$ , when all fit parameters are set to values corresponding to solid spheres; a similar behavior is expected for nonspherical particles. For illustration purposes, all variables are normalized to their respective values when  $\nu = 2$ . We infer that  $N_0$  shows the greatest sensitivity with respect to  $\nu$ , which becomes more accentuated at smaller values of  $\nu$ , while IWC and IWP, respectively, only vary within 10% for the entire range of values of simulated width parameters. While both  $N_0$  and  $D_0$  decrease when  $\nu$  increases, the opposite trend is visible for IWC and IWP. The conclusion of such analysis is that IWC and IWP will not be greatly influenced by the choice of the width parameter, thus making them reliable when comparing against measured data. The opposite is true for both  $N_0$  and  $D_0$ . We can thus expect large biases when comparing against measured data. Only additional information regarding the particle size distribution can alleviate this problem.

## 4. Error Analysis

[27] In this section we offer a discussion of the errors of the state vector and derived quantities. The basic assumption in the formulation of the cost function (1) is that model and observation errors are Gaussian in nature and uncorre-

lated. In the following section we will shed some light on errors due to possibility of biased model parameters. Since the level of errors is strongly dependent on both the degree of uncertainty of forward model input (i.e., measurements and model parameters) as well as their absolute values, we limit our discussion to relevant cases. Whenever necessary, estimates of error levels will be made to support our conclusions.

[28] We begin our error analysis by identifying the vector of model parameters as

$$\mathbf{b} = [\nu, S, f_A, g_A, f_Z, g_Z, C, D, \delta z, \beta_{\text{Rayl}}] \quad (28)$$

where we identify specific lidar and radar parameters introduced above as well as the distance  $D$  from lidar to target, and lidar Rayleigh backscatter  $\beta_{\text{Rayl}}$ . It is clear that this is a general representation; for example the lidar model does not explicitly depend on parameter  $f_Z$ . If  $\mathbf{B}$  is the model parameter error covariance matrix and  $\mathbf{Y}$  is the measurement error covariance matrix, then the observation error covariance matrix is

$$\mathbf{R} = \mathbf{Y} + \left( \frac{\partial \mathbf{H}}{\partial \mathbf{b}} \right)^T \mathbf{B} \left( \frac{\partial \mathbf{H}}{\partial \mathbf{b}} \right). \quad (29)$$

Inspection of (5) and (29) shows that errors in the model parameters and measurements can have different contributions to errors of state vector components, depending on a multitude of factors. These factors are due to evaluation of (5) involving estimations of several partial derivatives of the forward model  $H$  with respect to either state vector or model parameters. Given the complexity of our forward model, general conclusions regarding the propagation of errors cannot be drawn. However, we identify the following model parameters as main sources of errors:  $S$ ,  $\nu$ ,  $f_A$ , and  $f_Z$ . To simplify our discussion, we assume that only one parameter at the time is uncertain, and thus evaluate the level of uncertainty that it propagates into the retrieved state vector.

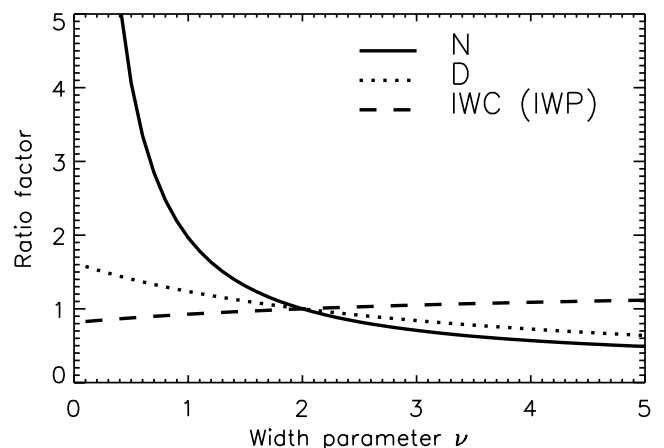


**Figure 3.** Normalized functional dependence of retrieved variables with respect to  $\nu$ . All fit coefficients are those for solid spheres. See text for details.

As a practical example, we choose the radar model. Using (18) we deduce that a  $\Delta f_Z$  uncertainty induces an uncertainty

$$\Delta Z \approx 10 \left[ \log_{10} D_0 + 0.43 \frac{1}{\Gamma(\nu + f_Z)} \frac{\partial \Gamma(\nu + f_Z)}{\partial f_Z} \right] \Delta f_Z \quad (30)$$

in the evaluation of the reflectivity field. Assuming a 10% error in  $f_Z$ , the above equation yields a value of  $\pm 3.3$  dBZ when  $D_0 = 0.03$  mm and all other parameters have defined values. When  $D_0 = 0.1$  mm, errors are reduced to  $\mp 2.2$  dBZ. Beside the change of sign in the above uncertainty, which is important for evaluating cross-correlation errors, we note that its level is greater than measurement error of  $\pm 1$  dBZ. In a similar way we can calculate that a 10% uncertainty in  $g_Z$  only yields  $\pm 1$  dBZ, while a 10% error in  $\nu$  is responsible for a  $\pm 3$  dBZ reflectivity error. The same exercise can be applied to the lidar equation. Given its similarity to the radar equation we expect the same behavior. We continue by investigating errors in  $D_0$  due to errors in  $Z$ , expressed as

$$\frac{\Delta D_0}{D_0} = \frac{\Delta Z}{10 f_Z}. \quad (31)$$

Thus a 3 dBZ reflectivity error is associated with a 7% error in characteristic diameter. For particle number concentration, the error can reach 30%. However, exact calculations must account for all possible correlations, while considering contributions from all components of the observation error covariance matrix (29).

[29] Beside the state vector components, for which we have error estimates, we can also compute errors for any derived quantity. We refer here to the optical depth, or the ice water content, expressed simply as

$$\delta V = \sqrt{\left( \frac{\partial V}{\partial \mathbf{x}} \right)^T \mathbf{S} \left( \frac{\partial V}{\partial \mathbf{x}} \right) + \left( \frac{\partial V}{\partial \mathbf{b}'} \right)^T \mathbf{B}' \left( \frac{\partial V}{\partial \mathbf{b}'} \right)}, \quad (32)$$

where  $V$  is the functional expression of our derived quantity in terms of the state vector  $\mathbf{x}$  and some additional parameters  $\mathbf{b}'$ . Like before,  $\mathbf{B}'$  is the error covariance matrix associated with these additional parameters. As an example, it can be shown that a 5% error in exponent  $f_m$  is responsible for a 40% error in computed IWC when  $D_0 = 0.02$  mm, that reduces to 25% when  $D_0 = 0.1$  mm. We thus expect very large errors of the derived quantities.

[30] We end our error analysis by noting that the lidar forward model, given the assumption of a constant  $S$ , limits the retrieved optical depth to values around three. This can be easily demonstrated by integrating the lidar equation to yield

$$S = [1 - \exp(-2\tau)] \left[ \int_0^H \beta' dz \right]^{-1}. \quad (33)$$

We see that when  $\tau = 3$ ,  $S$  must be known with 4 decimals precision; a value of  $\tau = 4$  requires 5 decimals precision, while  $\tau = 2$  only requires 3 decimals precision. Here we make the approximation that the denominator does not vary much within these limits of  $\tau$ , which is a relative good approximation for this kind of evaluation. Practical examples on the importance of  $S$  on retrieval can be found

in the work of *Stephens et al.* [2001]. We must also mention that the addition of MS effects slightly increases the upper retrievable limit of the optical depth, thus the importance of these effects when penetrating thicker clouds. Again, as mentioned before, the computed errors are no longer symmetric when uncertainties in  $S$  (or  $\tau$ ) becomes large. Thus as lidar penetrates deeper into the cloud, the errors of the retrieved cloud optical properties become larger and larger, due to the two-way attenuation factor via the uncertainties in  $S$ . In fact, for optical depths larger than about two, from the analysis above, uncertainties in  $S$  are the leading source of errors in our retrieved variables. It is also an indication that the lidar system is more sensitive to errors than the radar system (which in this case does not require a two-way attenuation correction factor). However, in principle, the level of errors can be lowered if additional information is available (i.e., knowledge about lidar ratio vertical profile and particle size distribution, independent optical depth and/or radiometric measurements, better knowledge about fit parameters, etc.).

[31] The purpose of the above exercises was to demonstrate that for nonlinear systems, the propagation of errors is highly dependent on both the vector state and specific model parameters. Thus general conclusions regarding the error covariance matrix cannot be easily drawn. Of concern here are also errors due to biases, which in a real case scenario go undetected. Depending on the biased variable, these errors can be larger than those associated with measurements errors. Thus the forward model needs to be reformulated in order to compensate for such errors. This can be done only by using experimentally derived forward model parameters, that are specific to the observed cloud system, with emphasis on any relevant vertical description. Owing to its universality, the optimal estimation technique is ideal for such a setting.

## 5. Application to CRYSTAL-FACE Data

[32] The Cirrus Regional Study of Tropical Anvils and Cirrus Layers–Florida Area Cirrus Experiment (CRYSTAL-FACE) campaign took place in southern Florida in the summer of 2002. During this campaign, measurements of convection, anvils and other tropical cirrus clouds were obtained with a combination of active and passive sensors aboard six research aircraft based in Key West and at two ground sites in southern Florida. The following subsections briefly describe the main characteristics of this observing system. Direct application of the proposed algorithm and comparison against in situ data collected during the flight of 26 July 2002 of the CRYSTAL-FACE experiment is presented. A following paper will present results obtained from analysis of other flight days and will attempt to compare the retrievals to other forms of data.

### 5.1. Remote Sensing of Cirrus: Lidar-Radar Observing System

[33] Cloud data from two active instruments aboard the ER-2 high-altitude research aircraft were used in this study. Lidar data were obtained from the Cloud Physics Lidar (CPL) that also flew aboard the ER-2 during CRYSTAL-FACE (<http://cpl.gsfc.nasa.gov>). The CPL is a pulsed lidar system that simultaneously transmits at 355, 532, and

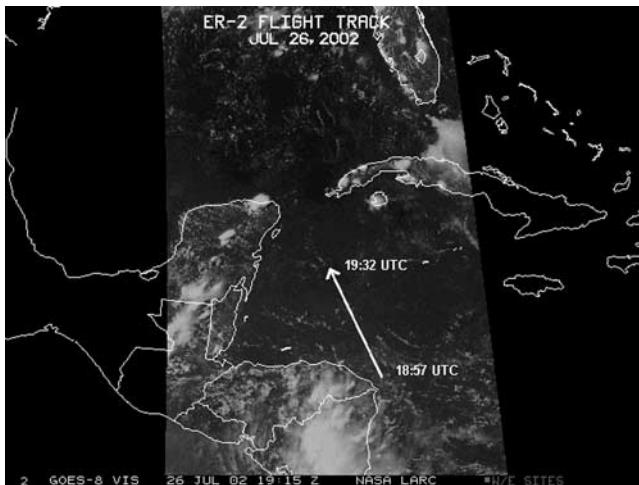


**Figure 4.** GOES-8 visible spectra image. ER-2 flight track is superimposed.

1064 nm; only the 532 nm visible channel was used in this study. The lidar's full angle FOV is  $100 \mu\text{rad}$ , thus multiple scattering effects are considerably reduced, but cannot entirely be neglected. During CRYSTAL-FACE, the CPL was able to observe many cases of thin to subvisible cirrus that contained particles too small to be observed by the cloud radar. The vertical resolution of the processed data is approximately 30 m vertical with a temporal resolution of 1 s. The radar data are from the 94 GHz Cloud Radar System (CRS, <http://meso-a.gsfc.nasa.gov/912/radar> [Li *et al.*, 2004]). The CRS is a W-band Doppler radar with a peak transmitting power of 1.7 kW and a minimum detectable signal of approximately  $-35$  dBZ at 15 km altitude and  $-20$  dBZ at the surface. Although this is sufficient to observe a large distribution of cirrus, as shown by McGill *et al.* [2002], the system misses a considerable fraction of optically thin cirrus. The raw radar data has a vertical resolution of 37.5 m and a temporal resolution of

approximately 0.5 s, and the data has been averaged with a  $5 \times 5$  ( $150 \text{ m} \times 2 \text{ s}$ ) moving window.

[34] For processing by the current retrieval algorithm, the attenuated backscatter from the lidar was matched, both spatially and temporally, to the radar reflectivity. This required regridding of both data sets. The radar data were regridded to the time resolution of the lidar (1.3 s) and the lidar data were regridded to the height resolution of the radar (37.5 m). In addition, both radar and lidar data were processed by a clutter removal algorithm that removed noncloud returns by comparing each data pixel to all surrounding pixels and removing those pixels that fell below a chosen noise threshold.

## 5.2. 26 July Case Study Description

[35] On 26 July 2002, the ER-2 high-altitude research aircraft flew a flight track from Key West to just off the coast of Nicaragua. This case study is concerned with the return flight leg toward the north-northwest, when the ER-2 flew over a cirrus shield located off the Nicaraguan coast. This cirrus was also being sampled in situ by the lower flying WB-57 aircraft. Ice water contents determined by the Harvard water vapor instrument through much of this cloud are nearly coincident with radar and lidar data measured by instruments on the ER-2. The ER-2 maintained a nearly constant altitude of approximately 20 km during this leg. Figure 4 shows the flight track superimposed on the visible GOES-8 satellite image.

[36] The cirrus shield that was sampled between approximately 18:10 and 19:10 UTC was associated with active convection over Nicaragua. This case study focuses on a 6 min window of observations that were collected late in the period, during which time the cloud layer was approximately 3.5 km thick. Nadir radar reflectivity, which has been processed to remove clutter as described earlier, and lidar attenuated backscatter for this flight leg are shown in Figure 5. The ER-2 plane maintained an airspeed of approximately 205 m/s during this case study, thus 1 min of time represents a distance of just over 12 km.

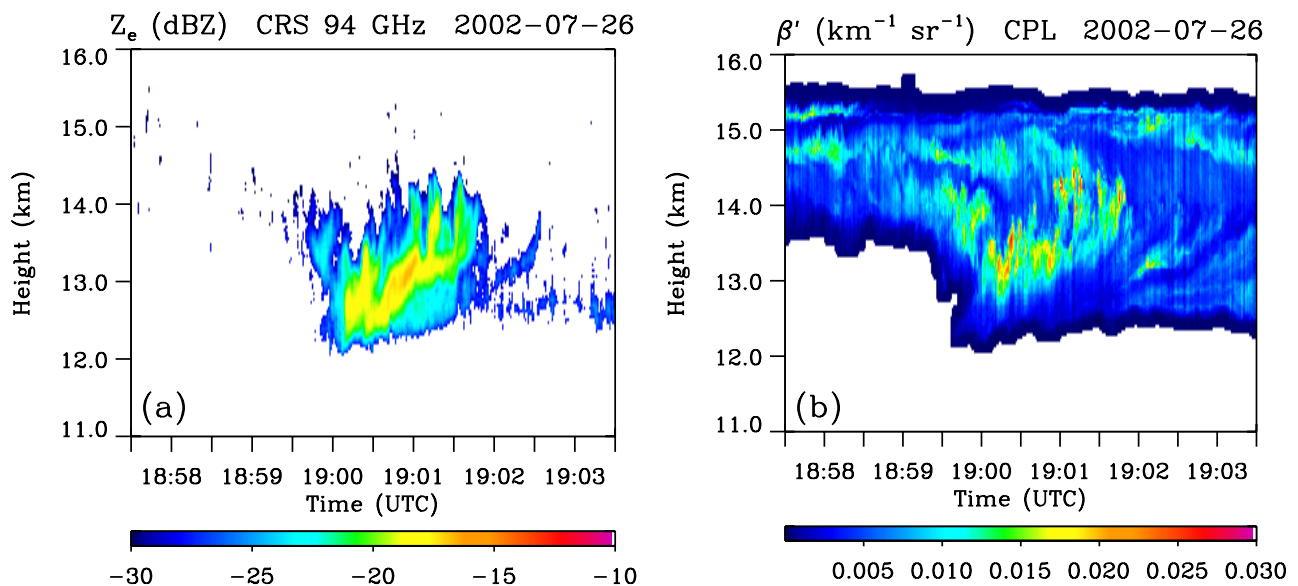


**Figure 5.** (a) CRS 94 GHz radar data and (b) CPL 532 nm lidar data on 26 July 2002.

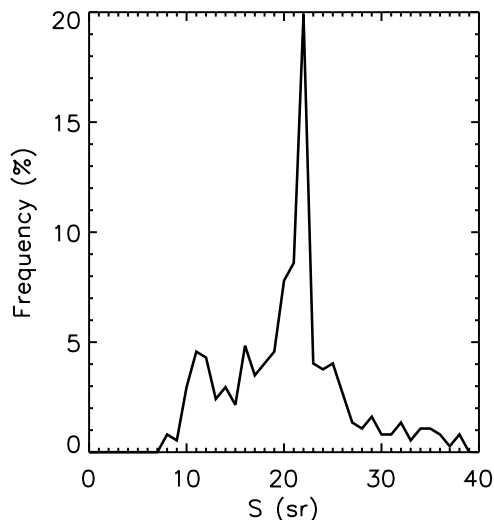


**Figure 6.** Probability distribution function of lidar ratio  $S$  on 26 July 2002.

[37] Although fairly extensive in vertical extent, the cirrus were optically thin as determined by lidar observations (with retrieved optical depth between 0.2 to 1.5), with cloud tops located near the tropopause level. The complementary nature of the lidar and radar observations are apparent in Figure 5. The radar observes only that portion of cloud containing the largest ice crystals, near cloud base. Detected radar reflectivities in this case vary from approximately  $-30$  to  $-17$  dBZ. The lidar observes nearly the entire cirrus layer in this observation window, but tends to attenuate quickly in thicker clouds. As previously mentioned, lidar ratio  $S$  was also estimated using GLAS algorithm. The values of  $S$  used in this case study are represented in Figure 6 in the form of a probability distribution function (PDF). From the figure we note that  $S$  ranges between 7 and 40 sr with a sharp peak around 22 sr, thus its importance on the retrieval as explained above.

[38] That portion of the cirrus with overlapping radar and lidar observations is the focus of this case study. It was one of few cases during the entire CRYSTAL-FACE campaign where radar and lidar data were available coincidentally with sufficiently nearby in situ observations within the overlap region.

### 5.3. In Situ Measurements of Cirrus

[39] During the time segment selected for algorithm validation, the ER-2 and WB-57 were vertically stacked to within an offset of approximately 3 km horizontally and 1 min in time. The WB-57 flew underneath the ER-2 and through the cloud that was observed by the radar and lidar.

[40] Ice water content data for the flight were obtained by the Harvard Total Water Instrument (TWI) onboard the WB-57 aircraft [Weinstock *et al.*, 1994]. The TWI collects ice particles into an inlet and funnels them through a heated chamber whereby they undergo a phase change and are transformed into vapor. The water vapor content of this moistened air above that of the ambient surroundings is therefore a measure of the IWC of the air that is sampled. Ice water volume mixing ratio data were obtained at 10 s

intervals, and were converted to IWC using measured pressure and temperature for comparison with the retrieval.

[41] In situ observations of the size spectra were provided by the SPP-100 scattering spectrometer (SPP), also mounted on the WB-57. The SPP measures the concentration of ice particles in 19 bins with sizes between 2 and 53.9  $\mu\text{m}$  by applying Mie theory to the light that is forward scattered by cloud particles. Forward scattering probes are known to have a number of biases, including overestimation of number concentration due to sampling of light scattered by particles larger than the probe is designed to measure [e.g., Heymsfield and McFarquhar, 1996]. However, composite size spectra derived from the CAPS (Cloud Aerosol and Precipitation Spectrometer), CPI (Cloud Particle Imager) and SPP-100 on the WB-57 indicate that the ratio of the concentrations of particles greater than 60  $\mu\text{m}$  in size to those less than 60  $\mu\text{m}$  was less than 2% during the entire case study period on 26 July [Garrett *et al.*, 2003]. We can conclude that the cirrus cloud under investigation was primarily composed of relatively small ice crystals, validating our assumptions. In anticipation of the discussion of the retrieval results, we briefly present the methodology used for such a comparison. The SPP data was used to calculate the number concentration and characteristic diameter of an equivalent Gamma particle size distribution with  $\nu = 2$  (as it is assumed by the lidar-radar model):

$$D_0^{(\text{SPP})} = \frac{1}{4} \cdot \frac{\langle D^3 \rangle}{\langle D^2 \rangle}, \quad (34)$$

where the means are calculated from the measured particle size distributions. We thus establish a common basis for comparison against lidar-radar retrieved characteristic diameter and particle number concentration. More retrieval results are presented in the following subsection.

### 5.4. Retrieval Results

[42] In areas where radar was not sensitive enough to observe thin cirrus, lidar observations alone was used to retrieve the vertical profile of extinction coefficient. Profile of the extinction coefficient for the case study considered here is presented in Figure 7a. From the figure we note that the extinction coefficient is a relatively smooth field with some sharp variations in regions where radar signal was measurable, indicating possible enhanced microphysical processes. The mean extinction coefficient is around  $0.3 \text{ km}^{-1}$ , reaching up to values around  $2 \text{ km}^{-1}$  in the overlap areas.

[43] By adding radar information to the lidar observing system, we are able to infer vertical profiles of  $D_0$ ,  $N_0$ , and IWC via the  $Z - \beta$  algorithm described above. The results of this algorithm applied to the CRYSTAL-FACE data are shown in Figures 7b, 7c, and 7d. For the overlap regions, the retrieved values of  $D_0$  ranges between 0.005 and 0.1 mm, indication of relatively small ice crystals. The mean value is centered at about 11  $\mu\text{m}$ , which yields an effective ice crystal radius of about 22  $\mu\text{m}$ . This is in support of our assumption regarding the size of the ice particles used in the estimation of MS effects. The particle number concentration  $N_0$  shows a large domain of variation with retrieved values of up to  $10^4$  particles per liter. While smaller values are naturally detected at cloud boundaries, there are regions in cloud displaying large vertical variations of this parameter,

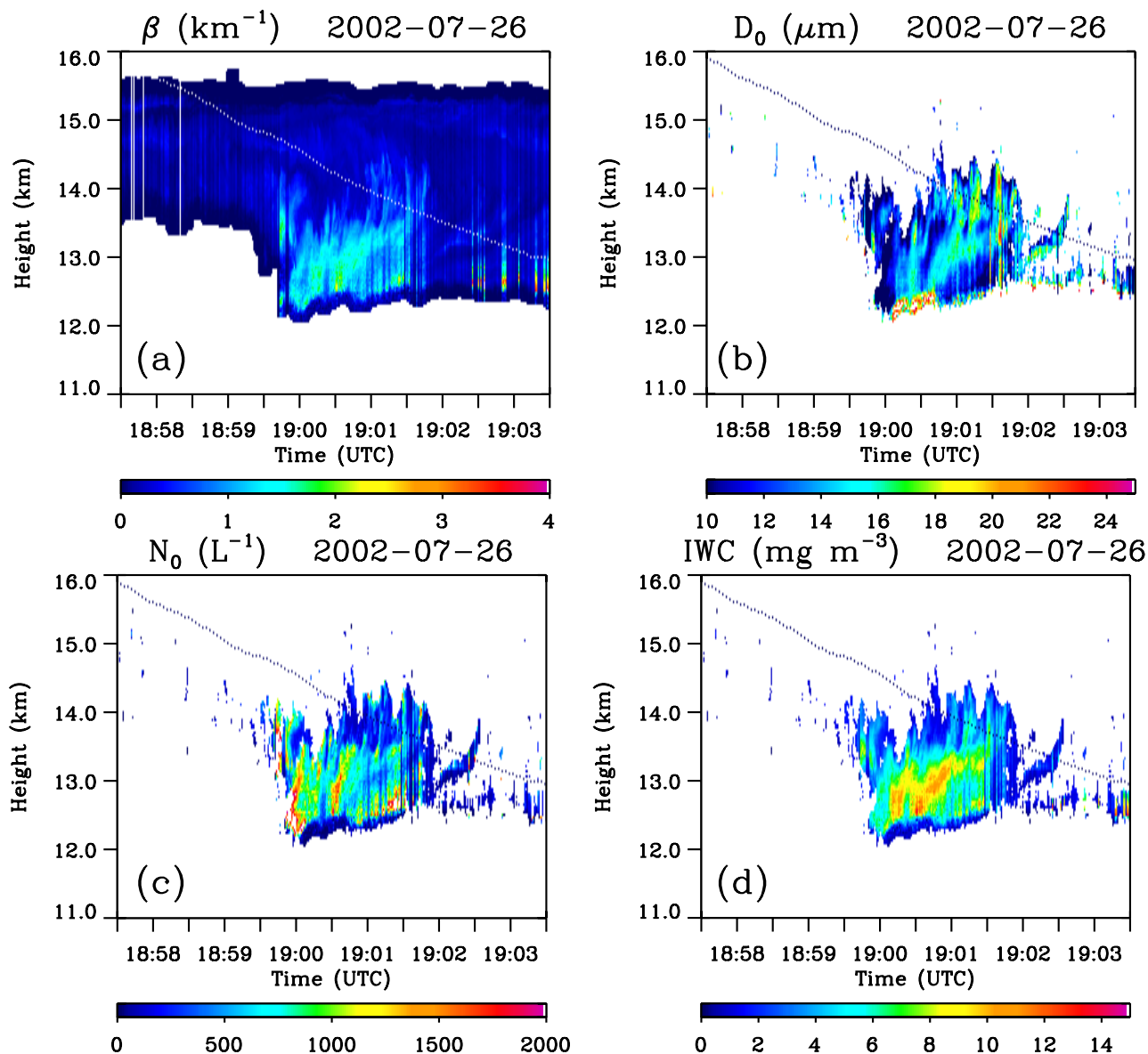


**Figure 7.** Time-height plots of retrieved (a) extinction coefficient  $\beta_{\text{ext}}$ , (b) characteristic diameter  $D_0$ , (c) particle number concentration  $N_0$ , and (d) IWC. Superimposed is the WB-57 flight altitude for these colocated observations.

underlying once more the importance of vertical profiling of clouds. Although not visible from these plots, there is a relatively close correlation between these two microphysical parameters. Finally, the computed IWC varies between 0.1 and 10  $\text{mg m}^{-3}$ , displaying a pattern that is closely related to the radar reflectivity. These correlations will be studied further below.

[44] Owing to uncertainties in both measurements and model parameters, the retrieved quantities are subject to errors. The relative errors as calculated by the optimal estimation method, are shown in Figure 8. From the figure, we see that errors in all fields increase dramatically at the far end of the cloud, where the lidar signal becomes uncertain, due to beam attenuation. At these locations, errors can exceed 100% in all retrieved fields. Of the retrieved variables,  $N_0$  shows the largest errors while  $D_0$  and  $\beta_{\text{ext}}$  display only a relatively small degree of uncertainty. In the

case of IWC, the dramatic increase in errors at the far end of the cloud is partly due to the fact that this is a derived quantity, influenced by the large uncertainties in  $N_0$  field. The main source of errors comes from uncertainties of the model parameters, amplified by the two-way transmittance term in the lidar model. Moreover, all these errors may be subject to bias errors, but this is a problem yet to be solved. However, for optically thin regions of the cloud, the errors are within reasonable limits, not exceeding 10% of the retrieved field. We conclude that overall, the retrievals are satisfactory from this point of view and hope that additional measurements and improved information about model parameters will further lower the level of these errors.

[45] We now extend the discussion started in the previous subsection by comparing our retrieved variables against the in situ measurements. The values of retrieved variables are considered to be coincidental with measurements if they are

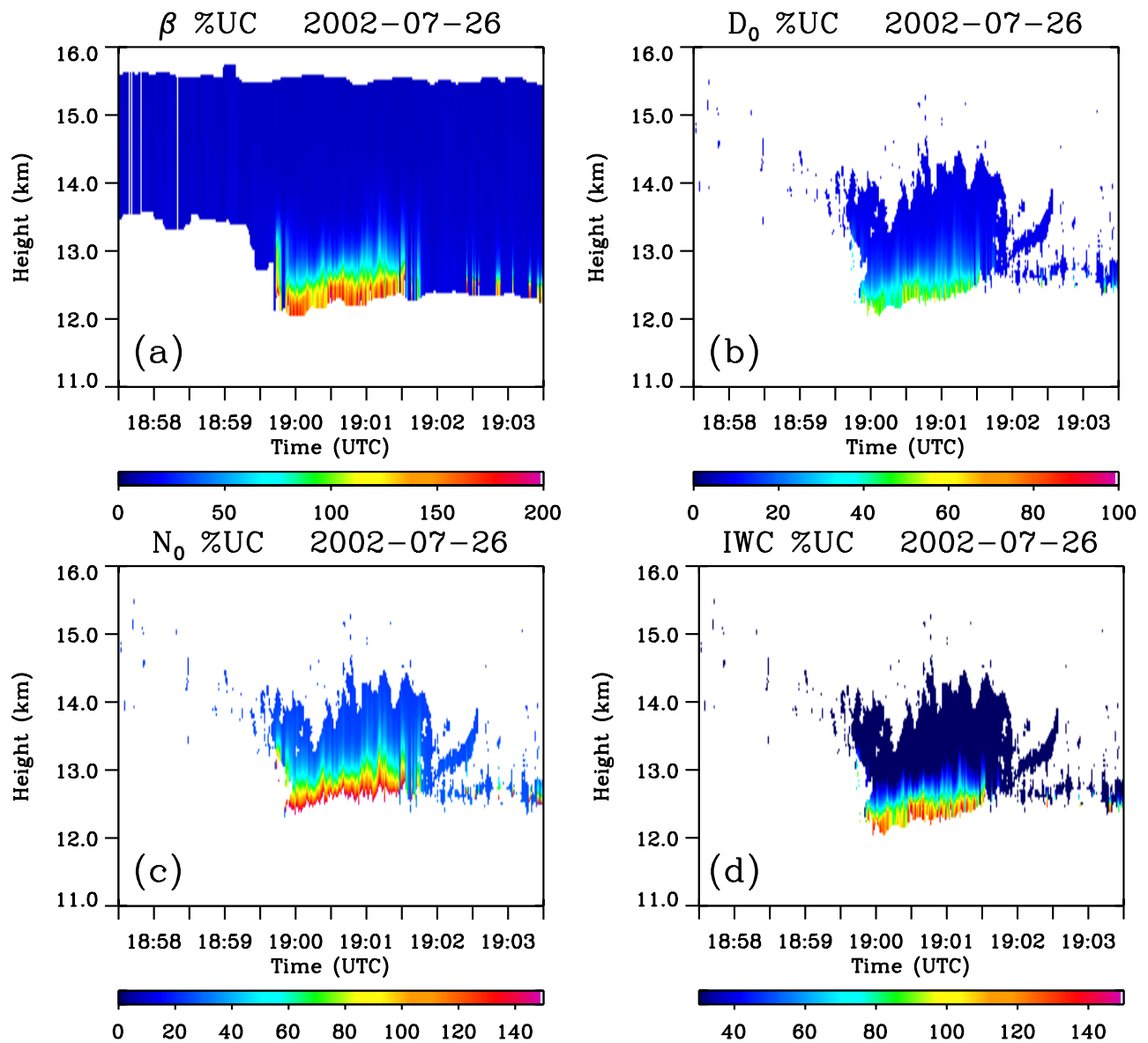


**Figure 8.** Time-height plots of relative errors of retrieved (a) extinction coefficient  $\beta_{\text{ext}}$ , (b) characteristic diameter  $D_0$ , (c) particle number concentration  $N_0$ , and (d) IWC.

within one range gate of the reported WB-57 altitude. We begin by investigating a particular event, then analyze the entire cloud penetration.

[46] The particular case focuses on the SPP data measured at 19:00:24 UTC. Figure 9 shows the number concentration as measured by the SPP probe (solid lines) and the associated Gamma distribution deduced as explained in the previous subsection (dots), where  $D_0^{(\text{SPP})} = 6.8 \mu\text{m}$ , and  $N_0^{(\text{SPP})} = 212$  particles per liter. We can clearly see that the assumption of a Gamma particle size distribution with  $\nu = 2$  is not the best choice in modeling the observed particle size distribution. In fact, a better choice for this particular case would be achieved for  $\nu = 1.8$ . However, in comparing the retrievals results against measured data, we must also acknowledge the differences between the sizes of the sampling volumes. Moreover, the choice of a Gamma particle size distribution is convenient in the description of the lidar-radar model. With the

dashed line, we represent the Gamma particle size distribution as retrieved from the lidar-radar data, with the choice of fit parameters as explained before. The retrieved microphysical parameters for this case are:  $D_0 = 13.2 \mu\text{m}$  and respectively  $N_0 = 123$  particles per liter. The above values, as determined by the lidar-radar system, are such that the associated Gamma distribution closely matches the measured distribution of larger particles, as can be seen from the figure. We refer here to particles with characteristic diameter around and larger than  $15 \mu\text{m}$ . This is indeed true since these particles contribute more to the radar signal than the smaller particles, which further explains the longer tail of the retrieved Gamma distribution. However, since the SPP probe indicates smaller ice crystals, using the above arguments we can determine an equivalent Gamma particle size distribution valid for solid ice spheres (i.e., smaller ice crystals). By simply using (17) with fit parameters adjusted for solid ice spheres, we deduce that the characteristic diameter of such an equivalent distribution

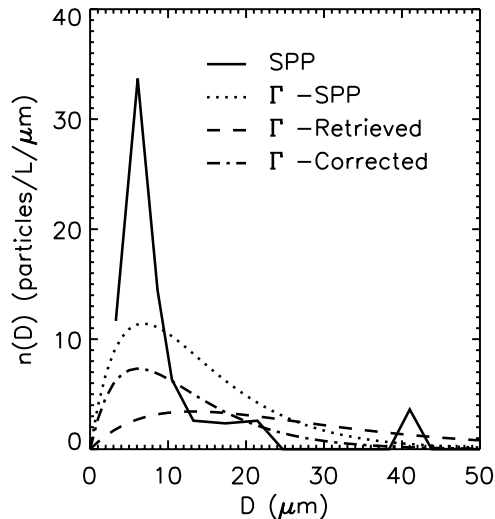


**Figure 9.** Particle size distribution from SPP probe (solid line), equivalent Gamma distribution (dotted line), retrieved Gamma distribution (dashed line), and retrieved Gamma distribution with correction for small particles (dash-dotted line).

of solid ice spheres is related to the one assuming nonspherical effects as

$$D_0^{(s)} = 0.67 D_0^{0.87}. \quad (35)$$

The above equation is nothing more than the application of the definition of equivalent spheres (9). Recasting the problem in this way, the Gamma particle size distribution of the equivalent solid ice spheres is represented with dash-dotted line. This new form of distribution is closer to the

one deduced from the measurements, and correctly accounts for density effects applied in the description of the lidar-radar observing system. The conclusion of this exercise is that small particles are not retrieved correctly by the lidar-radar system. This is probably due to the fact that both bimodal and density effects cannot be entirely captured by the definition of a single Gamma particle size distribution, nor by the assignment of fixed values for the fit parameters. The IWC is largely unaffected by this problem since it has been shown to display very little sensitivity to the specification of  $\nu$ ; in fact we can consider the retrieval of IWC as an interpolation problem since its exponent is somewhere between the exponents of the lidar and radar systems. Conversely the retrieval of number concentration and characteristic diameter can be seen as an extrapolation problem, and is thus prone to larger sensitivities to the distribution width  $\nu$ . We thus expect a better evaluation of this microphysical parameter.

[47] Figure 10 shows a comparison over the entire cloud penetration, where symbols represent measurements and lines retrieved variables. The IWC, as measured by the TWI instrument, slowly varies between 1 and 4  $\text{mg m}^{-3}$ , with the retrieved IWC values in close range, although showing a more dynamic variation from one point to another. A similar behavior is observed for both  $N_0$  and  $D_0$ , displayed in panels (b) and respectively (c) of the figure. As mentioned in the previous section, since small ice crystals dominate this top portion of the cloud, they are not properly retrieved by the lidar-radar algorithm that implicitly assumes larger ice crystals. The corrected  $D_0^{(s)}$  values are represented by the thin line and closely match the observed values. Overall, these results demonstrate the validity of our forward lidar-radar model, but also shows its limitations in detecting smaller ice crystals.

[48] For completeness, we also present the calculated values of cloud optical depth ( $\tau$ ), as seen by lidar, and ice

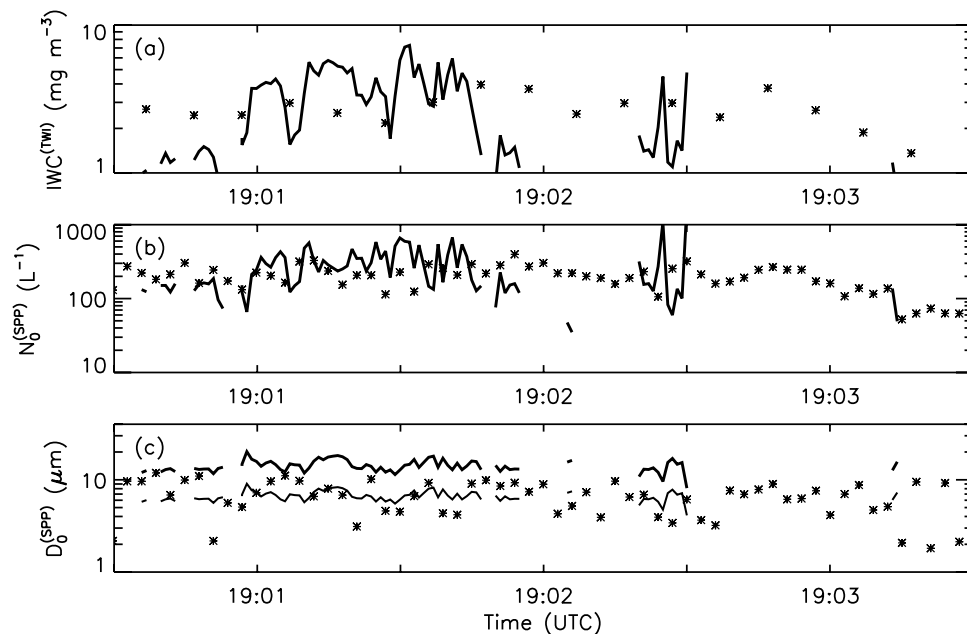


**Figure 10.** Observed and retrieved values of (a) IWC, (b) total particle number concentration, and (c) particle effective diameter. Solid lines show retrieved values, and asterisks show observations. The thin line in Figure 10c represents values of  $D_0^{(s)}$  of equivalent solid ice spheres. See text for details.

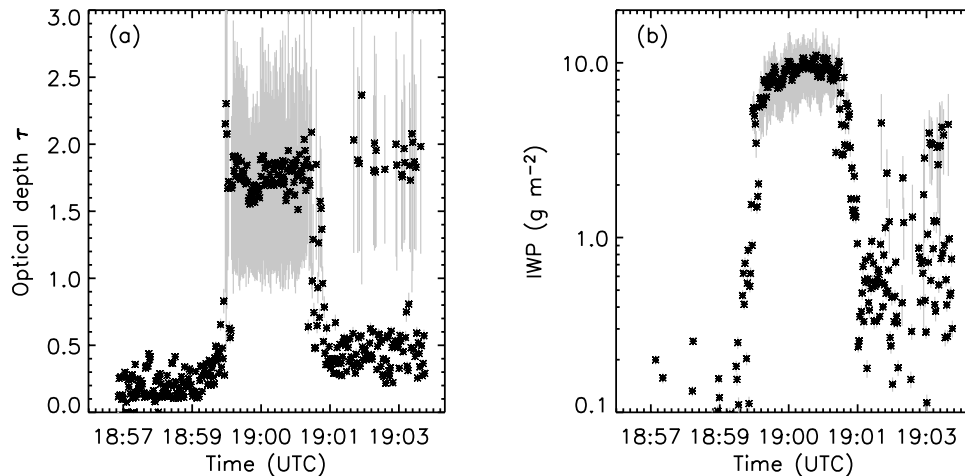


**Figure 11.** Calculated (a) optical depth  $\tau$  and (b) IWP. Associated errors are with shaded lines.

water path (IWP), valid only for the lidar-radar overlap region (see Figure 11). We note that the cirrus cloud is relatively thin and thus penetrated by lidar, with optical depth ranging from 0.2 to around 1.8. When radar signal is measurable, the IWP tops around  $10 \text{ g m}^{-2}$ , then, as radar signal fades out, it drops to values around  $2 \text{ g m}^{-2}$ , indication of a very thin cirrus cloud layer.

## 6. Validating Empirical Relationships

[49] We now shift focus on the possible correlations between various model variables as a possible way of validating results and/or improving model parameterization.

[50] Of interest is the relationship between the radar reflectivity  $Z$  and the ice water content IWC. In literature such a relationship is written as [e.g., *Brown et al.*, 1995]

$$\log_{10} \text{IWC} [\text{mg m}^{-3}] = c \cdot Z [\text{dBZ}] + d, \quad (36)$$

which is plotted in Figure 12a. The retrieval algorithm yields mean values of 0.073 and 2.24 for coefficients  $c$  and  $d$  respectively. Here we have filter out retrieved values of IWC with errors larger than 30%, occurring mostly at the far

end of the cloud, for reasons explained before. These fit coefficients are within the previously reported values [e.g., *Brown et al.*, 1995], thus further validating our results. However, the above relationship displays a relatively large variability, with values of IWC varying within one order of magnitude at a fixed value of  $Z$ . It must kept in mind that IWC is computed based on retrieved values of  $N_0$  and  $D_0$ , using an effective ice density, which probably is not valid over the entire ranges of observed particle sizes.

[51] If a relationship in the form of (36) is consider valid, then, from (23) and (18), we can speculate that a relationship between  $N_0$  and  $D_0$  is relevant. We must mention that such a relationship was also observed by *Heymtsfield et al.* [2002a]. Thus we can write that

$$N_0 [\text{L}^{-1}] = 10^B \cdot D_0^A [\mu\text{m}], \quad (37)$$

where  $A$  and  $B$  are empirical coefficients to be determined from the analysis of our lidar-radar system. As with (36), the above equation, if realistic, represents a property valid over several interacting cloud layers. We suggest that exponent  $A$  may indicate ice crystals growth regimes. For example, negative values of  $A$  are expected in regimes

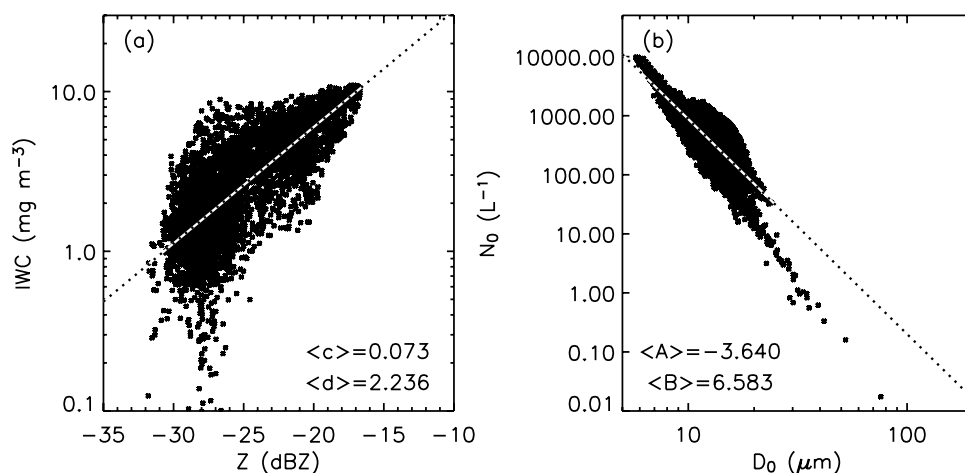


**Figure 12.** Scatterplots of (a) IWC versus  $Z$  and (b)  $N_0$  versus  $D_0$ . Mean values and analytical fits (dotted lines) are also represented. See text for details.

where aggregation (fragmentation) processes occur, when two or more crystals combine to form a larger crystal (or the reverse), yielding a negative correlation between  $N_0$  and  $D_0$ . In contrast, a positive value of  $A$  suggests a positive correlation between  $N_0$  and  $D_0$ , as might occur in vapor deposition/sublimation processes sustained by an advective transport. The scatter plot of  $N_0$  and  $D_0$  deduced from the  $Z - \beta$  model, presented on panel (b) of the figure, shows a strong correlation between these two microphysical parameters, suggesting that the proposed parameterization (37) may be valid. For the case studied, the mean values of the coefficients  $A$  and  $B$  are  $-3.64$  and  $6.58$  respectively. There is also strong evidence that coefficients  $A$  and  $B$  are linearly related supporting the idea that these coefficients describe specific microphysical processes. However, our findings are still preliminary and should also be tested against cloud models. We also note that  $A$  and  $B$  coefficients may depend on  $D_0$  (or  $N_0$ ) as well as cloud and thus be applicable within a given range. We mention again that  $D_0$  and  $N_0$  retrieved by this algorithm are related to the lidar-radar system itself, thus only partially matching the corresponding ice cloud microphysical properties, as explained in a previous subsection. With these problems aside, it may be possible to use the above parameterization together with a single radar or lidar measurement to infer both  $N_0$  and  $D_0$ , thus avoiding other constraints that must be imposed on either one of them [e.g., *Benedetti et al.*, 2003].

## 7. Summary and Conclusions

[52] A method for retrieving ice cloud optical and microphysical property profiles from millimeter cloud radar and lidar backscatter observations is introduced. We refer to this retrieval scheme as the  $Z - \beta$  algorithm and also introduce a variant of it, the  $\beta$  algorithm, that only uses lidar information. The lidar-radar models developed here account for the complex nature of cirrus clouds; in particular, nonspherical effects due to ice crystals in cirrus clouds are parameterized through the use of area-, volume- and mass-diameter empirical relationships. Moreover, the lidar model estimates multiple scatter contributions, while the radar model accounts for Mie effects.

[53] The retrieval of cirrus cloud optical and microphysical properties follows a scheme that is framed within the optimal estimation method. A modification to this method is provided to deal with large systems of high dimensionality. This modification greatly speeds up the iteration to solution and improves the accuracy of the final solution. It was also found that due to the different sensitivities of the radar and lidar observing systems, it is almost impossible to run the algorithm on both types of data at once. The best approach is to process the lidar data first, obtain an estimated extinction coefficient profile (and cloud optical depth) that later is resolved in terms of profiles of characteristic diameter  $D_0$  and number concentration  $N_0$  by adding radar information. For the overlap region, estimates of IWC and IWP can also be provided given the values of the above two microphysical parameters.

[54] Analysis of the lidar-radar model mathematical formulation along with results obtained from its direct application to real aircraft data collected during the CRYSTAL-FACE experiment, demonstrated the following.

[55] 1. The initial analysis of sensitivities and errors of the lidar-radar system indicates that IWC and  $D_0$  are most reliably retrieved, whereas  $N_0$  is the least reliable information derived from the retrievals. The latter was traced to the assumption of fixed values of size distribution width parameter and lidar ratio, that is,  $N_0$  is most sensitive to unretrieved microphysical assumptions. These sensitivities increase considerably at high cloud optical depths, when nonlinear effects become dominant. Future work should also consider an adequate treatment for bias corrections, associated with forward model parameters uncertainty, as tests have shown that this type of error can lead to large biases and errors in the retrieved fields. However, a compensation effect is observed, since for this observing system, some of the state vector components are somewhat correlated.

[56] 2. The application of the lidar-radar model to measured data collected during CRYSTAL-FACE experiment, underscores once more the need of better knowledge about model parameters, with a special interest in the fit coefficients that describe the nonspherical effects of ice crystal particles. Owing to the large variability in the values of these coefficients, large retrieval errors (and biases) are expected. For the case study examined, we set these coefficients to values that provide a reasonable balance between small and large particles, responsible for spherical and nonspherical effects. Future work should seek appropriate parameterization of these fit coefficients, thus providing more reliable retrievals for a large variety of cirrus cloud scenarios. Owing to the generality of the proposed retrieval algorithm, such implementations require minimal changes to the existing code.

[57] 3. Vertical profiles of  $N_0$ ,  $D_0$ , and IWC deduced using CRYSTAL-FACE data show a complex, layered structure of the cirrus cloud microphysics. A weakness of the lidar-radar observing system is the low probability of having simultaneous, overlapping lidar and radar measurements. In practice only small portions of clouds were observed by the both systems. Lack of in situ measurements in these overlap regions lidar/radar observations made it almost impossible to assess the performance of the retrievals and statistical approaches for validation are required. However, the comparison of the retrievals against measured data showed that the lidar-radar system is inefficient in detecting small ice crystals, but is geared instead toward cloud averaged microphysical parameters. As above, better choice of the fit parameters along with a bimodal description of the particle size distribution may solve this problem.

[58] 4. The investigation of empirical relationships between various cloud parameters indicates a distinct relationship between  $N_0$  and  $D_0$  that might offer insight into the nature of the microphysical processes taking place in cirrus. However, these results are preliminary and detailed in situ measurements of this effect are required. The IWC- $Z$  relationship derived in this particular case further confirms similar previously reported behavior, thus validating the method.

[59] The lidar-radar observing system described in this paper holds particular relevance to the Earth Observing System (EOS) CloudSat [*Stephens et al.*, 2002b] and Cloud-Aerosol Lidar and Infrared Pathfinder Satellite Observations satellite missions (<http://www-calipso.larc.nasa.gov>), scheduled for launch in Spring 2005. Flying in tight formation (separated by 15–60 s and lidar/radar

footprint congruency of less than 2 km with a goal of 50% footprint overlap) behind EOS-Aqua as part of the so-called A-Train constellation, the collective observing system will provide unprecedented opportunities to examine the detailed vertical properties (critical to describing the vertical distribution of atmospheric heating/cooling) of cloud systems globally. From the perspective of computational burden, the hybrid retrieval technique outlined in this paper is well suited (through its reduction of state vector dimensionality) to addressing the large data volumes associated with these global observations. Lessons learned from the A-Train research satellite constellation and its synergy of lidar, radar, and passive radiometer systems will augment dramatically our current understanding of clouds and cloud processes while forging a pathway toward the eventual operational use of these systems on future platforms.

[60] **Acknowledgments.** This research was funded by NASA Research grant NAG5-11475. The first author is grateful for the help received from the Cooperative Institute for Research in the Atmosphere (CIARA), which partially supported this research, while a postdoctoral fellow at Colorado State University, Department of Atmospheric Science. We also gratefully acknowledge the support of our research sponsor, the Office of Naval Research under program element PE-0602435N. The authors are thankful to L. Li and D. Hlavka of Goddard Space Flight Center for providing radar and lidar data, E. M. Weinstock of Harvard University for the TWI data, and P. Lawson of Spec, Inc. for the SPP-100 data.

## References

- Austin, R. T., and G. L. Stephens (2001), Retrieval of stratus cloud microphysical parameters using millimeter-wave radar and visible optical depth in preparation for CloudSat: 1. Algorithm formulation, *J. Geophys. Res.*, *106*, 28,233–28,242.
- Benedetti, A., G. L. Stephens, and J. M. Haynes (2003), Ice cloud microphysics retrievals from millimeter radar and visible optical depth using an estimation theory approach, *J. Geophys. Res.*, *108*(D11), 4335, doi:10.1029/2002JD002693.
- Bissonnette, L. R. (1988), Multiple scattering of narrow light beams in aerosols, *Appl. Opt.*, *27*, 2478–2484.
- Bohren, C. F., and D. R. Huffman (1983), *Absorption and Scattering of Light by Small Particles*, 530 pp., John Wiley, Hoboken, N. J.
- Brown, P. R. A., and P. N. Francis (1995), Improved measurements of the ice water content in cirrus using a total-water probe, *J. Atmos. Oceanic Technol.*, *12*, 410–414.
- Brown, P. R. A., A. J. Illingworth, A. J. Heymsfield, G. M. McFarquhar, K. A. Browning, and M. Gosset (1995), The role of spaceborne millimeter-wave radar in the global monitoring of ice cloud, *J. Appl. Meteorol.*, *34*, 2346–2366.
- Cooper, S. J., T. S. L'Ecuyer, and G. L. Stephens (2003), The impact of explicit cloud boundary information on ice cloud microphysical property retrievals from infrared radiances, *J. Geophys. Res.*, *108*(D3), 4107, doi:10.1029/2002JD002611.
- Donovan, D. P., and A. C. A. P. van Lammeren (2001), Cloud effective particle size and water content profile retrievals using combined lidar and radar observations: 1. Theory and examples, *J. Geophys. Res.*, *106*, 27,425–27,448.
- Donovan, D. P., M. Quante, I. Schlimme, and A. Macke (2005), Use of equivalent spheres to model the relation between radar reflectivity and optical extinction of ice cloud particles, *Appl. Opt.*, *43*, 4929–4940.
- Dowling, D. R., and L. F. Radke (1990), A summary of the physical properties of cirrus clouds, *J. Appl. Meteorol.*, *29*, 970–978.
- Eloranta, E. W. (1998), Practical model for the calculation of multiply scattered lidar returns, *Appl. Opt.*, *37*, 2464–2472.
- Francis, P. N., P. Hignett, and A. Macke (1998), The retrieval of cirrus cloud properties from aircraft multi-spectral reflectance measurements during EUCREX '93, *Q. J. R. Meteorol. Soc.*, *124*, 1273–1291.
- Garrett, T. J., H. Gerber, D. G. Baumgardner, C. H. Twohy, and E. H. Weinstock (2003), Small, highly reflective ice crystals in CRYSTAL-FACE anvil cirrus, *Geophys. Res. Lett.*, *30*(21), 2132, doi:10.1029/2003GL018153.
- Hartmann, D. L., and K. Larson (2002), An important constraint on the tropical cloud-climate feedback, *Geophys. Res. Lett.*, *29*(20), 1951, doi:10.1029/2002GL015835.
- Heidinger, A., and G. L. Stephens (2000), Molecular line absorption in a scattering atmosphere, part II: Application to remote sensing in the O<sub>2</sub> A-band, *J. Atmos. Sci.*, *57*, 1615–1634.
- Held, I. M., and B. J. Soden (2000), Water vapor feedback and global warming, *Annu. Rev. Energy Environ.*, *25*, 441–475.
- Heymsfield, A. J. (1972), Ice crystals terminal velocities, *J. Atmos. Sci.*, *29*, 1348–1357.
- Heymsfield, A. J., and G. M. McFarquhar (1996), High albedos of cirrus in the tropical Pacific warm pool: Microphysical implications from CEPEX and from Kwajalein, Marshall Islands, *J. Atmos. Sci.*, *53*, 2224–2451.
- Heymsfield, A. J., A. Bansemmer, P. R. Field, S. L. Durgen, J. L. Stith, J. E. Dye, W. Hall, and C. A. Grainger (2002a), Observations and parameterizations of particle size distributions in deep tropical cirrus and stratiform precipitating clouds: Results from in situ observations in TRMM field campaigns, *J. Atmos. Sci.*, *59*, 3457–3491.
- Heymsfield, A. J., S. Lewis, A. Bansemmer, J. Iaquinta, L. Miloshevich, M. Kajikawa, C. Twohy, and M. R. Poellot (2002b), A general approach for deriving the properties of cirrus and stratiform ice cloud particles, *J. Atmos. Sci.*, *59*, 3–29.
- Heymsfield, A. J., A. Bansemmer, C. Schmitt, C. Twohy, and M. R. Poellot (2004a), Effective ice particle densities derived from aircraft data, *J. Atmos. Sci.*, *61*, 982–1003.
- Heymsfield, A. J., C. G. Schmitt, A. Bansemmer, D. Baumgardner, E. Weinstock, J. T. Smith, and D. Sayres (2004b), Effective ice particle densities for cold anvil cirrus, *Geophys. Res. Lett.*, *31*, L02101, doi:10.1029/2003GL018311.
- Intrieri, J. M., G. L. Stephens, W. L. Eberhard, and T. Uttal (1993), A method for determining cirrus cloud particle sizes using a lidar and radar backscatter technique, *J. Appl. Meteorol.*, *32*, 1074–1082.
- Jazwinsky, A. H. (1970), *Stochastic Processes and Filtering Theory*, 376 pp., Elsevier, New York.
- Li, L., G. M. Heymsfield, P. E. Racette, L. Tian, and E. Zenker (2004), The 94 GHz cloud radar system on a NASA ER-2 aircraft, *J. Atmos. Oceanic Technol.*, *21*, 1378–1388.
- Lindzen, R. S., M. D. Chou, and A. Y. Hou (2001), Does the Earth have an adaptive infrared iris?, *Bull. Am. Meteorol. Soc.*, *82*, 417–432.
- Liou, K. N. (1986), Influence of cirrus clouds on weather and climate processes: A global perspective, *Mon. Weather Rev.*, *114*, 1167–1199.
- Matrosov, S. Y., M. D. Shupe, A. J. Heymsfield, and P. Zuidema (2003), Ice cloud optical thickness and extinction estimates from radar measurements, *J. Appl. Meteorol.*, *42*, 1584–1597.
- McGill, M. J., D. L. Hlavka, W. D. Hart, V. S. Scott, J. D. Spinhirne, and B. Schmid (2002), Cloud physics lidar: Instrument description and initial measurement results, *Appl. Opt.*, *41*, 3725–3734.
- McGill, M. J., D. L. Hlavka, W. D. Hart, E. J. Welton, and J. R. Campbell (2003), Airborne lidar measurements of aerosol optical properties during SAFARI-2000, *J. Geophys. Res.*, *108*(D13), 8493, doi:10.1029/2002JD002370.
- Miller, S. D., G. L. Stephens, and R. T. Austin (2001), GOES 10 cloud optical property retrievals in the context of vertically varying microphysics, *J. Geophys. Res.*, *106*, 17,981–17,995.
- Mitchell, D. L., A. Macke, and Y. Liu (1996), Modeling cirrus clouds. Part II: Treatment of radiative properties, *J. Atmos. Sci.*, *53*, 2967–2996.
- Mitrescu, C. (2005), Lidar model with parameterized multiple scattering for retrieving cloud optical properties, *J. Quant. Spectrosc. Radiat. Transfer*, *94*, 201–224.
- Ramanathan, V., and W. D. Collins (1991), Thermodynamic regulation of the ocean warming by cirrus clouds deduced from observations of the 1987 El Niño, *Nature*, *351*, 27–32.
- Rodgers, C. D. (2000), *Inverse Methods for Atmospheric Sounding: Theory and Practice*, 238 pp., World Sci., Boca Raton, Fla.
- Stephens, G. L. (1994), *Remote Sensing of the Lower Atmosphere*, 523 pp., Oxford Univ. Press, New York.
- Stephens, G. L. (2002), Cirrus, climate and global change, in *Cirrus*, edited by D. K. Lynch et al., pp. 433–448, Oxford Univ. Press, New York.
- Stephens, G. L. (2005), Cloud feedbacks in the climate system: A critical review, *J. Clim.*, *18*, 237–273.
- Stephens, G. L., R. J. Engelen, M. Vaughan, and T. L. Anderson (2001), Toward retrieving properties of the tenuous atmosphere using space-based lidar measurements, *J. Geophys. Res.*, *106*, 28,143–28,157.
- Stephens, G. L., et al. (2002), The CloudSat mission and the A-Train: A new dimension of space-based observations of clouds and precipitation, *Bull. Am. Meteorol. Soc.*, *12*, 1771–1790.
- Verlinde, J., P. J. Flatau, and W. R. Cotton (1990), Analytical solutions to the collection growth equation: Comparison with approximate methods and application to cloud microphysics parameterization schemes, *J. Atmos. Sci.*, *47*, 2871–2880.
- Weinstock, E. M., et al. (1994), New fast response photofragment fluorescent hygrometer for use on the NASA ER-2 and the Perseus remotely piloted aircraft, *Rev. Sci. Instrum.*, *65*, 3544–3554.

Weikamp, C. (1999), *Lidar Measurements: Atmospheric Constituents, Clouds, and Ground Reflectance*, 614 pp., Springer, New York.

---

J. M. Haynes and G. L. Stephens, Department of Atmospheric Science, Colorado State University, Fort Collins, CO 80523, USA. (haynes@atmos.colostate.edu; stephens@atmos.colostate.edu)

G. M. Heymsfield and M. J. McGill, NASA Goddard Space Flight Center, Greenbelt, MD 20771, USA. (gerald.heymsfield@nasa.gov; mcgill@virl.gsfc.nasa.gov)

S. D. Miller and C. Mitrescu, Marine Meteorology Division, Satellite Meteorological Application Section, Naval Research Laboratory, 7 Grace Hopper Avenue, MS 2, Monterey, CA 93943-5502, USA. (miller@nrlmry.navy.mil; mitrescu@nrlmry.navy.mil)